



# Understanding and correcting wavenumber error in interference pattern structured illumination imaging

**BENJAMIN G. WHETTEN,<sup>1,2</sup> JAROM S. JACKSON,<sup>1,3</sup>  RICHARD L. SANDBERG,<sup>1</sup>  AND DALLIN S. DURFEE<sup>4,\*</sup>**

<sup>1</sup>*Department of Physics and Astronomy, Brigham Young University, Provo, UT 84602, USA*

<sup>2</sup>*Current affiliation Department of Physics, University of Colorado, Boulder, CO 80309, USA*

<sup>3</sup>*Current affiliation Navy Surface Warfare Center, Panama City, FL 32407, USA*

<sup>4</sup>*Department of Physics, Utah Valley University, Orem, UT 84058, USA*

\**dallin.durfee@uvu.edu*

**Abstract:** The impacts of uncertainty in mirror movements in mechanically scanned interference pattern structured illumination imaging (IPSII) are discussed. It is shown that uncertainty in IPSII mirror movements causes errors in both the phase and amplitude of the Fourier transform of the resulting imaging. Finally, we demonstrate that iterative phase retrieval algorithms can improve the quality of IPSII images by correcting the phase errors caused by mirror movement uncertainties.

© 2021 Optica Publishing Group under the terms of the [Optica Open Access Publishing Agreement](#)

## 1. Introduction

In interference pattern structured illumination imaging (IPSII), high resolution images of extended objects can be obtained by measuring transmitted or reflected light from structured illumination with a single pixel detector (often a photomultiplier tube or a diode). This is accomplished by projecting interfering coherent waves with different patterns onto an object. By measuring the total amount of light transmitted through or reflected from the object for each pattern, an image of the object can be calculated [1]. The use of interference to generate the patterns enables high resolution imaging without the need of high numerical aperture imaging elements. While IPSII interference patterns can be generated and scanned in numerous ways [2–7], here we use mechanical angle scan IPSII (MAS-IPSII) in which the angles between interfering beams are controlled and scanned using motorized mirror mounts [1,8–10].

While similar to other structured illumination imaging methods [11,12], there are several advantages of IPSII imaging. For example, as with other lensless imaging techniques [13,14], the resolution and depth of field are not subject to the limits of conventional imaging [1,15–17]. In addition, because IPSII does not require high numerical aperture optics to produce high resolution images, and because it requires only single pixel detectors, it could be used with waves for which high quality multi-pixel detectors and imaging optics are hard to obtain or difficult to work with; for example, with the extreme UV and x-ray regimes.

Our experimental methods are detailed in [1,8] and are summarized here. As shown in Fig. 1, the interference patterns are created using a Mach-Zehnder Interferometer. Mechanically rotated mirrors change the angle between the interfering beams in two dimensions to create sinusoidal interference patterns with different spatial frequencies. A photodetector behind the object measures the total power of the light transmitted through the object for each pattern.

Using a mirror mounted on a piezoelectric stack in one arm of the interferometer we sweep the phase of the interference pattern, causing a sinusoidal oscillation detectable with the photodetector. From the amplitude and phase of this oscillation, the Fourier coefficient corresponding to the spatial frequency of the interference pattern can be determined. By making measurements with

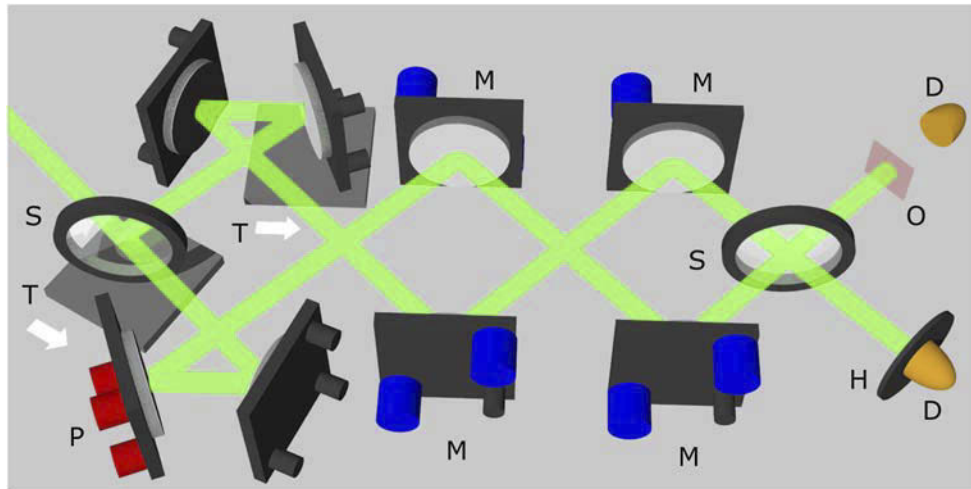


**Fig. 1.** A modified Mach-Zehnder interferometer is created using a pair of beamsplitters (labelled "S" in the figure) and eight mirrors. The object to be imaged (labelled "O") is placed in one of the interferometer outputs and a reference pinhole ("H") is placed in the other. Photodetectors ("D") measure the light transmitted through the object and the pinhole. Four of the mirrors ("M") are on motorized mounts, allowing us to change the angle of each beam while keeping their position on the object constant. One of the mirrors is mounted on a piezoelectric stack ("P"), allowing us to scan the phase of the interferometer. One mirror and one beamsplitter are mounted on translation stages ("T"), allowing us to balance the path lengths of the interferometer.

many different interference patterns, we can obtain a Fourier-space representation of the object. Taking an inverse Fourier transform then produces an image of the object.

Because the overall phase of the interferometer is prone to drift, a second photodetector is placed behind a reference pinhole in the other interferometer output. The pinhole is smaller than the width of a single interference fringe in the highest spatial frequency patterns. As the phase of the interferometer is swept, the oscillating signal from this photodetector tells us the phase of the interference pattern at the corresponding location on the object, such that the phase of each Fourier coefficient be found from the relative phase of the oscillating object signal and the oscillating reference signal.

MAS-IPSII images taken by Jackson [8] showed significant ghosting near the edges of the field of view. Figure 2 contains an image of the measured 1951 USAF resolution test chart (Thorlabs R1DS1N) where ghosting is clearly seen on the left side of the image. Jackson hypothesized that this distortion may be caused by  $k$ -space, or wavenumber, errors [8]. These errors in the wavenumber of the Fourier transform are likely caused by uncertainties in the movements of the rotating mirrors in the experimental IPSII setup. In this work, we seek to confirm Jackson's [8] hypothesis that wavenumber error causes ghosting and other noise in MAS-IPSII images and seek to correct or repair these ghosting effects numerically. To do so, we simulate wavenumber position errors using a modified discrete Fourier transform and show that iterative phase retrieval algorithms can be applied to IPSII images to partially correct the ghosting caused by wavenumber errors.

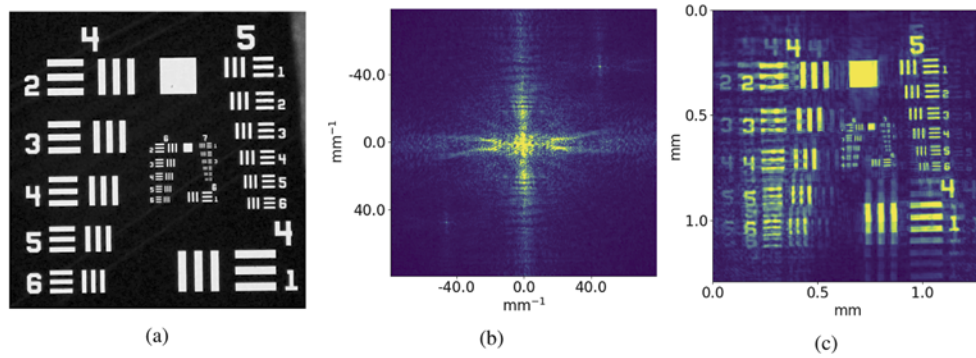


**Fig. 2.** (a) Optical microscope image of the portion of the 1951 USAF resolution test chart imaged in our experimental MAS-IPSII tests. (b) Experimental MAS-IPSII Fourier transform amplitude measurement of the test chart. (c) The resulting image after transforming the data from plot (b) into the image domain. Note the ghosting effects near the edges of the image.

## 2. Analysis of wavenumber error

In this section we analyze the impact of wavenumber error on IPSII images. First, we discuss how random mirror positioning errors in the IPSII interferometer lead to interference patterns with the wrong fringe spacing and thus incorrect Fourier amplitudes and phases. Next, we present a method of numerically simulating these wavenumber errors and their effect on both the phase and amplitude of IPSII images in Fourier space.

As discussed above, IPSII generates an image by projecting an interference pattern onto the object of interest while scanning the spatial frequency of the interference pattern [1–8]. The various spatial frequencies are obtained by adjusting the mirrors labeled "M" in Fig. 1. These mirrors are rotated using stepper motors, high thread count screws, and custom mounts that allow for precision movements [18]. However, mechanical errors caused by effects such as gear backlash and skipped steps create uncertainty in the movements of the interferometer mirrors. This uncertainty in the mirror movements leads to uncertainty in the spatial frequencies of the resulting interference pattern which in turn causes errors in the wavenumber sampling interval of the image data.

To more effectively study the impact of wavenumber error on IPSII images, we present a method of modeling this error. We first treat the error in the mirror movements as an uncertainty in the sampling of the true Fourier transform of the target object. The experimental process of IPSII is mathematically equivalent to finding the centered discrete Fourier transform of the imaged object,  $\mathcal{F}_{p,q}$ , on a size  $N$  by  $M$  array:

$$\mathcal{F}_{p,q} = \sum_{n=0}^{N-1} \sum_{m=0}^{M-1} F_{n,m} \exp \left[ -i2\pi \left( \frac{(p - \frac{N-1}{2})(n - \frac{N-1}{2})}{N} + \frac{(q - \frac{M-1}{2})(m - \frac{M-1}{2})}{M} \right) \right] \quad (1)$$

Here,  $F$  is the original object in image space,  $n$  and  $m$  are the pixel indices of the image, and  $p$  and  $q$  are the indices in wavenumber space.

The discrete Fourier transform normally requires evenly spaced data points; however, the uncertainty in mirror movements in MAS-IPSII leads to a sampling of the Fourier transform at irregular intervals. We represent this effect by modifying the discrete Fourier transform (Eq. (1))

to include random variations in wavenumber:

$$\mathcal{F}_{p,q} = \sum_{n=0}^{N-1} \sum_{m=0}^{M-1} F_{n,m} \exp \left[ -i2\pi \left( \frac{(p - \frac{N-1}{2} + \epsilon_{p,n,m})(n - \frac{N-1}{2})}{N} + \frac{(q - \frac{M-1}{2} + \epsilon_{q,n,m})(m - \frac{M-1}{2})}{M} \right) \right] \quad (2)$$

The  $\epsilon_{p,n,m}$  and  $\epsilon_{q,n,m}$  represent variations in the wavenumber caused by the random noise in mirror mount movements. We chose to use a Gaussian function to approximate the distribution for the variations  $\epsilon_{p,n,m}$  and  $\epsilon_{q,n,m}$ . Throughout the simulations, we characterize the strength of the wavenumber error by the unitless real-valued parameter  $\sigma$ , where  $\sigma$  is the standard deviation defining the width of the Gaussian distribution of wavenumber variations  $\epsilon_{p,n,m}$  and  $\epsilon_{q,n,m}$ . We

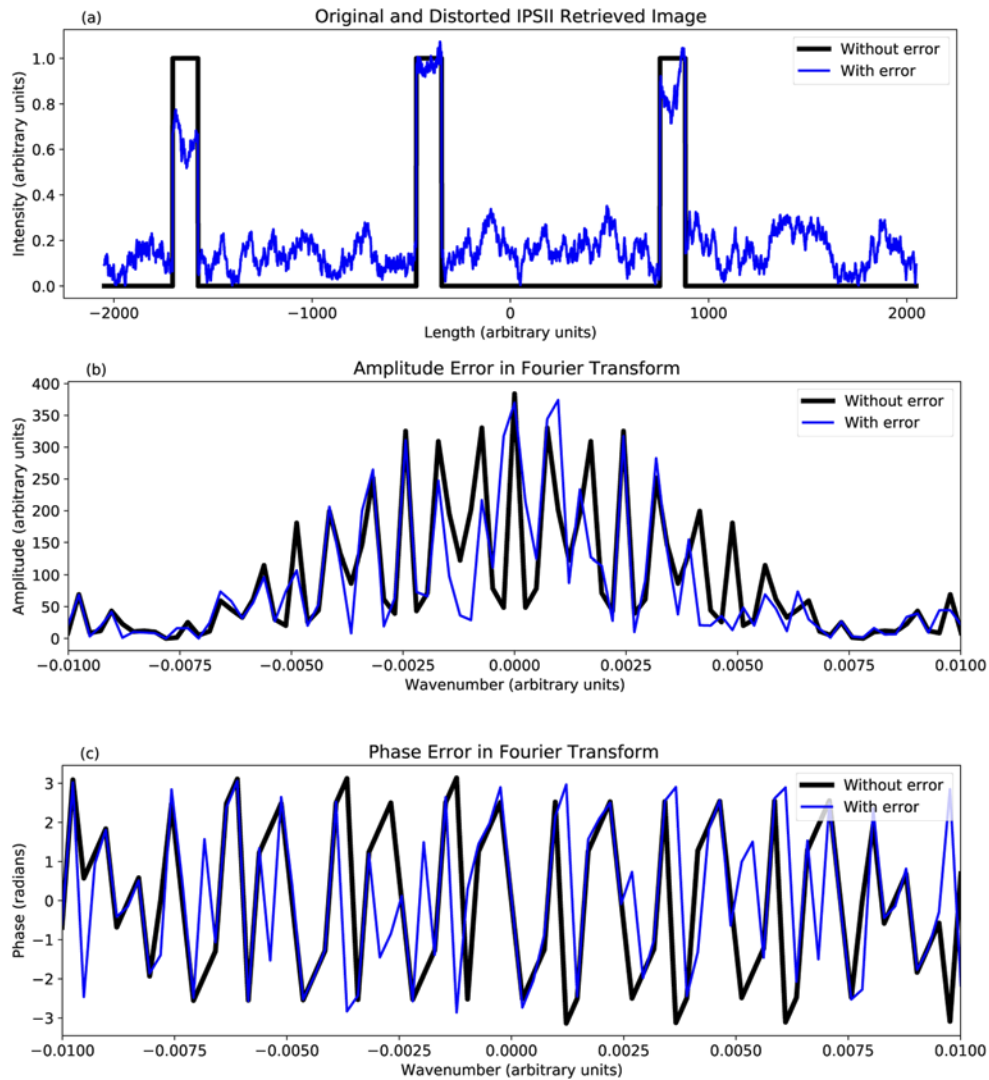


**Fig. 3.** Numerical simulation of an image distorted by simulated wavenumber errors with  $\epsilon = 0.4$ . (a) shows the original and 'IPSII retrieved' image after adding distortions, (b) shows a portion of the amplitude of the Fourier transform of the image, and (c) shows the phase over the same interval.

define  $\sigma$  and the  $\epsilon$  parameters as ratios of the wavenumber error to the wavenumber step size of the data.

To simulate the effects of mirror movement uncertainty, we first transform an image using Eq. (2) thus adding the corresponding errors  $\epsilon_{p,n,m}$  and  $\epsilon_{q,n,m}$ . Next, we transform the resulting distorted Fourier transform back to image space by first applying a phase ramp to shift the DFT data a half index in Fourier space and then applying an inverse Fast Fourier Transform (FFT). More details on the code used to implement this process are found here [9] and in Code 1, Ref. [19].

An IPSII measurement is analogous to computing the discrete Fourier transform (DFT) of the imaged target. The wavenumber errors caused by uncertainties in the mirror movements are then equivalent to performing a DFT with random, uneven spacing between the discrete wavenumbers. Thus, the wavenumber errors cause MAS-IPSII to sample the true DFT amplitude and phase of the image at uneven intervals. By comparing the distorted Fourier transform with the error-free version, these amplitude and phase errors become apparent. Figure 3 shows a one-dimensional numerical simulation of the effects of errors on three square pulses and the corresponding Fourier transform with and without simulated wavenumber errors. The effect in image space causes what appears to be random noise and distortions. In Fourier space, the phase and amplitude of the data are distorted somewhat but still have the same general shape as the undistorted transform due to the slowly varying nature of the phase and amplitude of the Fourier transform.

As shown by previous research, the phase of the Fourier transform contains most of the image information [20]. The errors in the phase of IPSII data are likely responsible for most of the distortions in the final image. Because of this, repairing the phase errors in the data would have a significant impact on the resulting image even with persisting amplitude errors.

### 3. Application of phase retrieval to IPSII

In this section, we demonstrate the application of iterative phase retrieval algorithms to IPSII images. We apply the Error Reduction (ER) [21,22], Hybrid Input-Output (HIO) [23] and shrink wrapping [24] phase retrieval techniques to IPSII and discuss their effectiveness [25].

Much research has been done in the field of phase retrieval techniques in the context of other imaging systems. For example, iterative phase retrieval techniques are commonly used in Coherent Diffraction Imaging (CDI) [26,27] to obtain the phase of a Fourier transform from its amplitude (often obtained from the square root of a measured diffraction pattern) and a priori knowledge of the image (such as, for example, the overall size of the object) [22,23,25,28]. IPSII requires slight modification of phase retrieval algorithms because IPSII already provides information on both the phase and amplitude of an image in Fourier space. However, as discussed in the previous section, these phases and amplitudes are distorted due to wavenumber error. Thus, with IPSII we apply phase retrieval techniques to refine the experimental measurements of the phase data rather than reconstruct the phase entirely from only the amplitudes. Another important consideration with IPSII is that phase retrieval algorithms will improve the phase data but leave the amplitudes unchanged. This means that the amplitude errors caused by wavenumber position errors will persist even after applying phase retrieval to IPSII images, possibly degrading the image quality.

The most basic phase retrieval method that we apply to IPSII is known as compact support or Error Reduction (ER) and was demonstrated initially by Gerchberg and Saxton, and more broadly later by Fienup [21–23]. As seen in Fig. 4, ER consists of iterating between image and Fourier space while applying two constraints each iteration: a finite size support constraint to the image and replacing the retrieved amplitude or modulus of the Fourier space data with the measured one. We show the workflow used for IPSII phase refinement in Fig. 4. Here  $F_0(x, y)$  represents the original measured IPSII image,  $F_n(x, y)$  is the  $n^{\text{th}}$  iteration of the image, and  $\mathcal{F}_{n+1}$  is the  $(n + 1)^{\text{th}}$  iteration of the Fourier transform that is used to create  $F_{n+1}$ . To begin the algorithm,

we manually determine a support region to use as a constraint on  $F_n(x, y)$ . This region should not contain any portion of the imaged object and instead be empty space. We then force the amplitude of  $F_n(x, y)$  to zero within this support region to generate  $F_{\text{con}}$ . Taking the FFT of this new constrained image creates  $\mathcal{F}_n$ . This new Fourier transform,  $\mathcal{F}_n$ , has phase values that better approximate the true error-free Fourier transform, but also has modified amplitude values as well. Next, we take only the phase data of  $\mathcal{F}_n$  and combine it with the experimental amplitude values as measured by IPSII to generate  $\mathcal{F}_{n,\text{con}}$ . By taking the inverse FFT of  $\mathcal{F}_{n,\text{con}}$ , we obtain a new image, labeled  $F_{n+1}$ , which has improved phase estimates. The original constraint can then be applied to this next generation image and the process repeated until it converges.

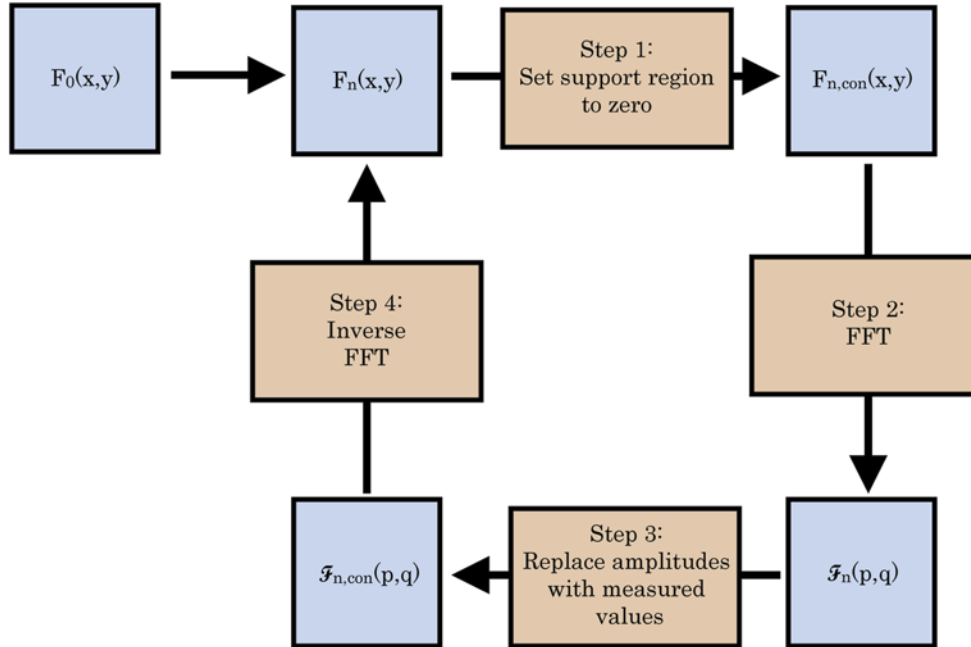


**Fig. 4.** Iterative method used by the Error Reduction algorithm to correct the phase of IPSII image data. A constraint is first applied to the experimental data and then the Fourier transform is taken. The phase of this new transform combines with the experimentally measured amplitudes to create a new Fourier transform. Finally, the inverse transform is taken returning a new version of the image that can be iteratively plugged back into the algorithm.

The ER algorithm quickly converges to a minimum in solution space; however, this minimum is likely not the desired global minimum [25]. To dislodge the phase retrieval algorithm from a local minimum, other methods aside from ER must be used. One of the most commonly used alternatives to ER is Hybrid Input-Output (HIO) [22]. HIO works similarly to the ER algorithm by iterating between image space and Fourier space while applying a modified compact image support constraint and the Fourier modulus constraint. The difference in the HIO compact support constraint method is that instead of fixing the support region at zero amplitude in image space, HIO reduces the intensity in this region more gradually. The HIO constraint as applied in this work is

$$I_{n+1}(x, y) = \begin{cases} I_n - \beta I_{n-1} & (x, y) \in \gamma \\ I_n & (x, y) \notin \gamma \end{cases}, \quad (3)$$

where  $I$  is the image intensity at location  $(x, y)$ . The symbol  $\gamma$  represents the support region surrounding the object in image space that would be set to zero intensity in the ER algorithm and  $\beta$  is a constant representing the strength of the constraint. For the simulations presented here,  $\beta$  was set to a value of 0.8.

HIO applies the constraint less aggressively than ER and is able to better explore the solution space and avoid local minima. However, HIO sometimes converges to a local minimum that does not trap ER and vice versa. For this reason, we have chosen to implement both algorithms to correct IPSII images, switching between the two periodically to minimize the likelihood of convergence to a local minimum [25].

Beyond HIO and ER, we have also implemented shrink wrapping to increase the convergence rate of the algorithm [24]. The shrink wrapping algorithm periodically increases the constraint region to include additional regions of the image that have near zero intensity. The process begins by first convolving the intensity of the image with a two-dimensional Gaussian function. The constraint region is then expanded to include any portion of the convolved image that falls below a set amplitude threshold. The width of the Gaussian used in subsequent shrink wrappings is reduced gradually as the image converges to a solution. We found that a reduction following a 1/8 power law gives good results. Additionally, the amplitude threshold of the shrink wrapping is gradually increased starting from a value of 10% up to value of 50% using the same 1/8 power law. The power law controls the rate at which the shrink wrapping threshold changes, with a 1/8 power law meaning that the shrink wrapping threshold is approximately equal to 10% until rapidly increasing to near 50%. Maintaining a low threshold until the final iterations prevents the shrink wrapping from erasing important image data before the ER and HIO algorithms are able to converge to a stable image. The optimal values of these parameters change slightly depending on the nature of the object being imaged and how much of the image background can be fixed to zero intensity.

The complete phase retrieval algorithm applied to MAS-IPSII images consists of a cycle of thirty iterations of HIO, thirty iterations of ER followed by a shrink wrap similar to recipes suggested elsewhere [29]. This complete cycle is repeated five times. Because the algorithm still sometimes fails to converge to the correct solution, random phase noise with a uniform distribution and up to  $\pm 0.5$  radians is added to the data to dislodge it from local minima after every 5 iterations of ER or HIO. The code used to implement the phase retrieval algorithm is included in [Code 2](#), Ref. [30].

We recognize that one of the most effective phase retrieval techniques is Guided Hybrid Input-Output [31], but it is not well suited to IPSII. Guided HIO involves carrying out HIO over successive generations which each include several reconstructions that start with a different random phase and selecting next generation of phases from the best result of the previous generation. However, when using phase retrieval with IPSII data, we begin with estimates of the initial phases instead of seeding the initial phases randomly as would normally be done with Guided HIO. Because we do not randomly seed the initial phases between individual attempts at HIO with the IPSII data, there is insufficient variation between individual trials to apply Guided HIO. For this reason, we have not used a guided approach for our IPSII phase retrieval code.

The effects of phase retrieval on an IPSII image are shown in Fig. 5. Subplot (a) shows the experimentally measured image with the constraint boundary marked in red, (b) zooms in on the relevant part of the data, (c) shows the data from (b) after phase retrieval using ER, HIO, and periodically adding random phase, and (d) shows the results of phase retrieval also including shrink wrapping at each repeated cycle as described above. The best results are obtained when shrink wrapping is used as seen in Fig. 5(d). Note that the ghosting seen in Fig. 5(a) has disappeared almost entirely in Fig. 5(d). The clearer separation between the bars in the lower left of the repaired image shows that the resolution has improved in that portion of the image. There are still some remaining artifacts of ghosting effects in Fig. 5(d), but they are limited to regions

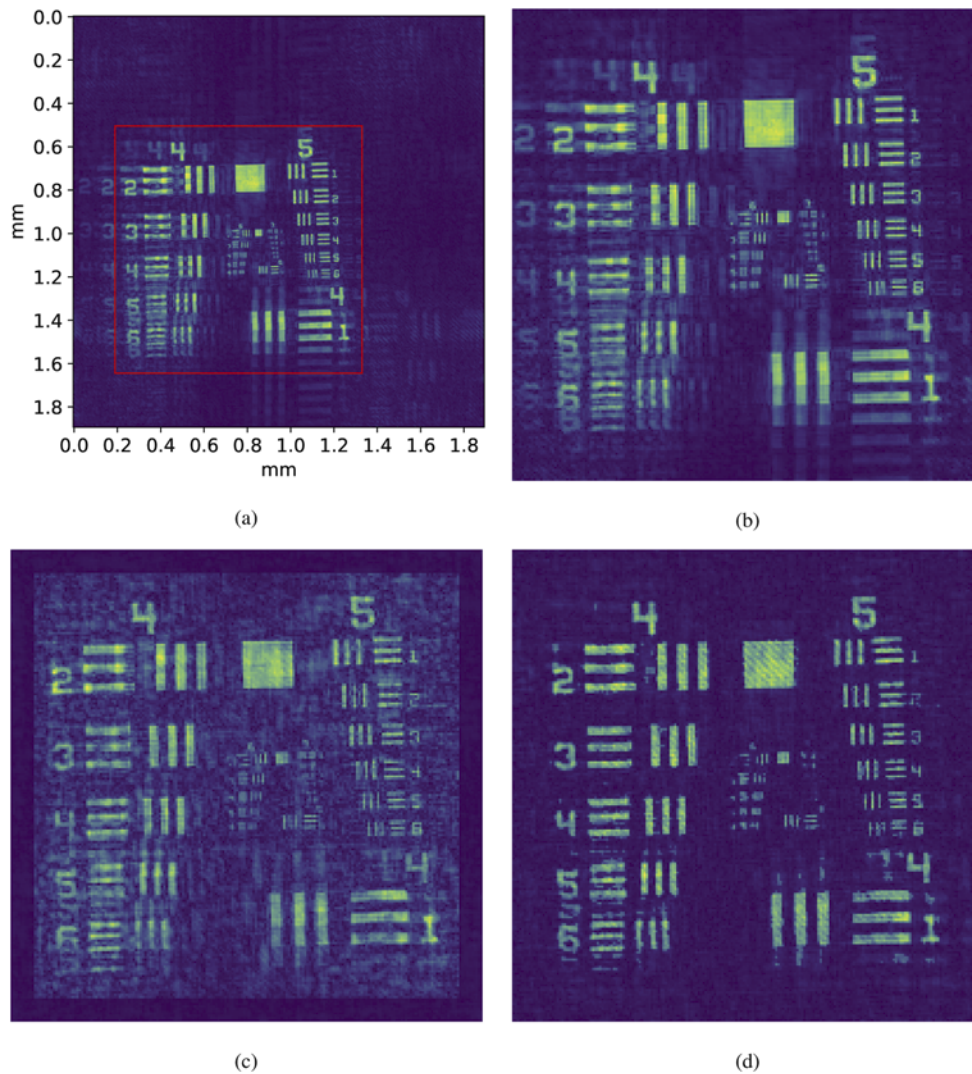


**Fig. 5.** Results of phase retrieval on an experimental MAS-IPSII image. (a) and (b) show an experimentally measured MAS-IPSII image of the 1951 USAF resolution test chart with the boundary of the support region shown in red in (a) and the region of interest shown in (b). (c) shows the same image after phase retrieval using ER, HIO, and random phase as described in the text while (d) shows the phase retrieval results after also including shrink wrapping.

with intense ghost images located near their respective truth images, such as with the vertical bars in group 4, element 1. Additionally, the phase retrieval process caused small distortions of the fine structures in the center of the target. However, the distortion introduced by the phase retrieval algorithm is at the single pixel level and thus does not significantly impact the image quality. Further optimization and tuning of the shrink wrap parameters may be able to reduce the distortion of these small details entirely in the phase-repaired images.

To quantify the effectiveness of phase retrieval algorithms in this application, we compare the average error present in IPSII images before and after phase retrieval. The error is calculated

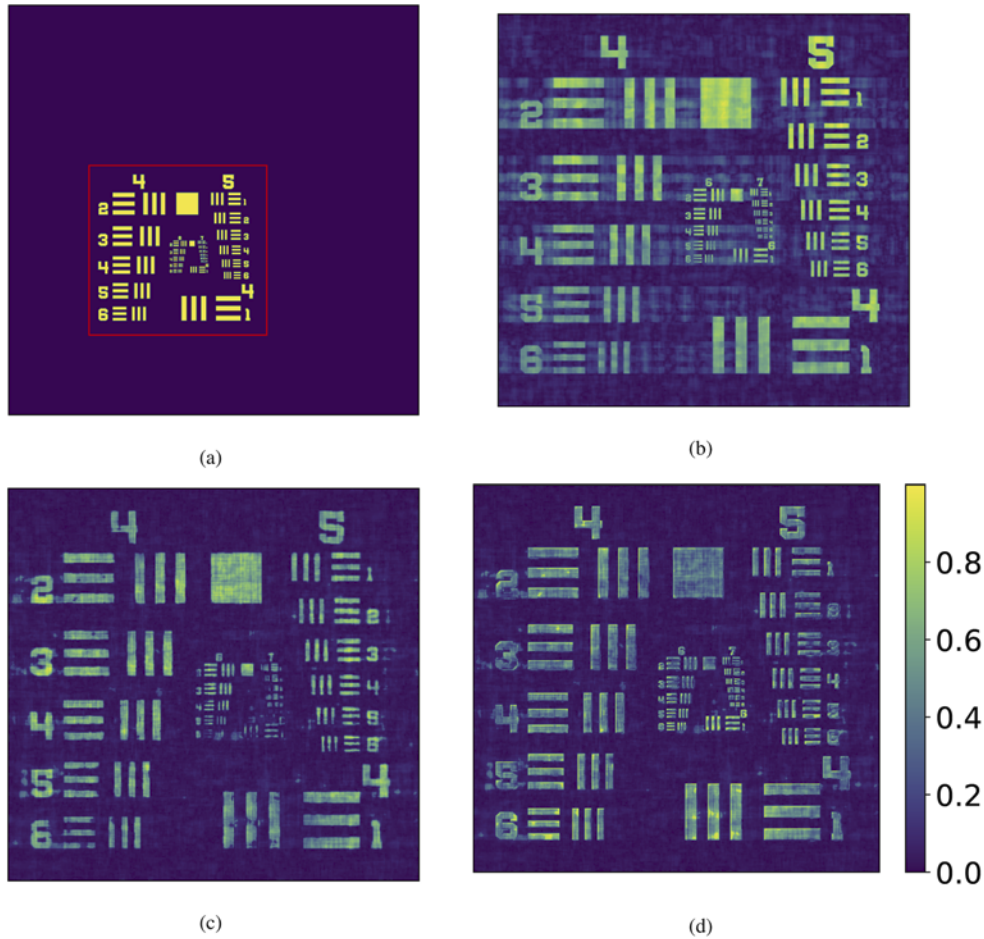


**Fig. 6.** Simulated MAS-IPSII Image with Phase Retrieval: (a) Bitmap reconstruction of groups 4 and 5 of the USAF 1951 Test Chart with support region boundary marked in red. (b) Region of interest of image (a) after simulating MAS-IPSII wavenumber distortions. (c) Image after phase retrieval. (d) Absolute error calculated for each pixel in the region of interest

using the mean absolute error (MAE):

$$\text{MAE} = \frac{\sum (I - I_0)}{N}, \quad (4)$$

where  $I$  is the pixel intensity of the distorted image and  $I_0$  is the pixel intensity of the undistorted original image. The sum is performed only over the region containing objects of interest, purposefully excluding the initial constraint region, and  $N$  is the number of pixels within this region of interest. The MAE gives an average error value that can be used to broadly define the quality of the image. This error calculation requires knowledge of the undistorted image, and thus, it is not easily applicable to experimental IPSII data where the undistorted image is unknown. This error calculation method can be more easily applied to simulated IPSII images distorted using Eq. (2) as seen in Fig. 6.

To calculate the MAE of a MAS-IPSII image before and after phase retrieval, we first constructed the bitmap representation of the USAF 1951 test chart seen in Fig. 6(a). To determine

an appropriate value for  $\sigma$  in our simulations, we referenced the results of Dallen Petersen, who found that the home-built MAS-IPSII mirror mounts used in the experiment have an average absolute error of 7.67 arc seconds with an approximate half Gaussian distribution [18]. Converting this average error value to the standard deviation for a full Gaussian and multiplying by a factor of  $\sqrt{4}$  for the four rotating mirrors used in the setup, we obtained a value  $\sigma = 0.476$ . Using this  $\sigma$  value, we simulated the effects of MAS-IPSII wavenumber error using Eq. (2). The resulting image is shown in Fig. 6(b). Figure 6(c) shows this same simulated data after phase retrieval (5 cycles of 30 iterations of ER, 30 iterations of HIO followed by a shrink wrap, with no random phase added). For this simulated MAS-IPSII data, the image before phase retrieval has an MAE of 0.128 and an MAE of 0.119 after phase retrieval. The decreased MAE value shows a small but measurable increase in the overall image quality. But more importantly, Fig. 6(c) shows significantly less ghosting after phase retrieval than Fig. 6(b). As seen in Fig. 6(d), most of the error that persists in the image after phase retrieval is due to variations in the intensity of the image, and not due to ghosting or other artifacts.

The few artifacts that persist in MAS-IPSII images even after phase retrieval are likely due to the amplitude errors in k-space that originate from the wavenumber error. We attempted to repair the amplitudes of IPSII images using an ER algorithm similar to what is shown in Fig. 4 but replacing the phases of  $\mathcal{F}_n$  in step 3 with the measured phases instead of replacing the amplitudes to generate  $\mathcal{F}_{n+1}$ . However, these initial attempts at amplitude retrieval did not lead to any improvement in the image quality.

#### 4. Conclusion

We have shown that errors in the wavenumber of the Fourier transform distort both the phase and amplitude of MAS-IPSII images in the Fourier domain. This means that small errors in the mirror movements in the MAS-IPSII interferometer will cause both phase and amplitude errors in the resulting Fourier transform data. The errors in the Fourier transform manifest in the resulting images as ghosting and distortions seen primarily near the edges of the field of view. Through the application of iterative phase retrieval algorithms, we have shown that it is possible to repair the phase of MAS-IPSII images to obtain higher quality images.

Some work can be done to improve the capabilities of our IPSII phase retrieval algorithm. In particular, optimizing the input parameters such as HIO strength and number of shrink wraps for the phase retrieval algorithms is currently difficult and time consuming. Future work could be done to implement a genetic algorithm that would find the optimal input parameters to streamline the phase retrieval process.

The phase retrieval method we propose demonstrates that iterative algorithms are effective at reducing the amount of ghosting seen in IPSII images. With additional refinement of the IPSII phase retrieval, the quality of IPSII images could be further improved and the impact of mirror movement uncertainty on IPSII could be minimized.

**Funding.** Utah Valley University; Brigham Young University.

**Acknowledgments.** We are grateful for the assistance of Carter Day and Dallen Petersen.

**Disclosures.** The authors declare no conflicts of interests.

**Data availability.** Data underlying the results presented in this paper are not publicly available at this time but may be obtained from the authors upon reasonable request.

#### References

1. J. Jackson and D. Durfee, "Mechanically scanned interference pattern structured illumination imaging," *Opt. Express* **27**(10), 14969 (2019).
2. M. Saxena, G. Eluru, and S. S. Gorthi, "Structured illumination microscopy," *Adv. Opt. Photonics* **7**(2), 241–275 (2015).
3. P. Kner, B. B. Chhun, E. R. Griffis, L. Winoto, and M. G. Gustafsson, "Super-resolution video microscopy of live cells by structured illumination," *Nat. Methods* **6**(5), 339–342 (2009).

4. O. Gliko, W. E. Brownell, and P. Saggau, "Fast two-dimensional standing-wave total-internal-reflection fluorescence microscopy using acousto-optic deflectors," *Opt. Lett.* **34**(6), 836–838 (2009).
5. V. I. Mandrosov, "Panoramic microscope with interfering illuminating beams," *Proc. SPIE* **3568**, 167–177 (1999).
6. M. S. Mermelstein, "Synthetic aperture microscopy," Ph.D. thesis, Massachusetts Institute of Technology (1999).
7. D. Feldkhun and K. H. Wagner, "Doppler encoded excitation pattern tomographic optical microscopy," *Appl. Opt.* **49**(34), H47–H63 (2010).
8. J. S. Jackson, "Mechanically scanned interference pattern structured illumination imaging," Ph.D. thesis, Brigham Young University (2019).
9. B. Whetten, "Wavenumber error in interference pattern lensless imaging," Senior thesis, Brigham Young University (2020).
10. C. F. Day, "Effects of illumination shadows in interference pattern structured illumination imaging," Senior thesis, Brigham Young University (2020).
11. Z. Zhang, X. Ma, and J. Zhong, "Single-pixel imaging by means of Fourier spectrum acquisition," *Nat. Commun.* **6**(1), 6225 (2015).
12. D. J. Higley, D. G. Winters, G. L. Futia, and R. A. Bartels, "Theory of diffraction effects in spatial frequency-modulated imaging," *J. Opt. Soc. Am. A* **29**(12), 2579–2590 (2012).
13. A. Ozcan and E. McLeod, "Lensless imaging and sensing," *Annu. Rev. Biomed. Eng.* **18**(1), 77–102 (2016).
14. A. Greenbaum, W. Luo, T.-W. Su, Z. Göröcs, L. Xue, S. O. Isikman, A. F. Coskun, O. Mudanyali, and A. Ozcan, "Imaging without lenses: achievements and remaining challenges of wide-field on-chip microscopy," *Nat. Methods* **9**(9), 889–895 (2012).
15. E. Abbe, "Beiträge zur theorie des Mikroskops und der mikroskopischen wahrnehmung," *Arch. f. Mikrosk. Anat.* **9**(1), 413–468 (1873).
16. M. G. L. Gustafsson, "Surpassing the lateral resolution limit by a factor of two using structured illumination microscopy," *J. Microsc.* **198**(2), 82–87 (2000).
17. J. T. Frohn, H. F. Knapp, and A. Stemmer, "True optical resolution beyond the Rayleigh limit achieved by standingwave illumination," *Proc. Natl. Acad. Sci. U.S.A.* **97**(13), 7232–7236 (2000).
18. D. Petersen, "Motorized mirror controller with 3D printed parts," Senior thesis, Brigham Young University (2020).
19. B. Whetten, "Supplemental information - computer code: Introduce error to simulated patterns," figshare (2021), <https://doi.org/10.6084/m9.figshare.16881772>.
20. A. V. Oppenheim and J. S. Lim, "The importance of phase in signals," *Proc. IEEE* **69**(5), 529–541 (1981).
21. R. W. Gerchberg and W. O. Saxton, "Practical algorithm for determination of phase from image and diffraction plane pictures," *Optik* **35**, 237–246 (1972).
22. J. R. Fienup, "Reconstruction of an object from the modulus of its Fourier transform," *Opt. Lett.* **3**(1), 27–29 (1978).
23. J. R. Fienup, "Phase retrieval algorithms: a comparison," *Appl. Opt.* **21**(15), 2758–2769 (1982).
24. S. Marchesini, H. He, N. Chapman, P. Hau-Riege, A. Noy, R. Howells, U. Weierstall, and H. Spence, "X-ray image reconstruction from a diffraction pattern alone," *Phys. Rev. B* **68**(14), 140101 (2003).
25. S. Marchesini, "A unified evaluation of iterative projection algorithms for phase retrieval," *Rev. Sci. Instrum.* **78**(1), 011301 (2007).
26. J. Miao, R. L. Sandberg, and C. Song, "Coherent x-ray diffraction imaging," *IEEE J. Select. Topics Quantum Electron.* **18**(1), 399–410 (2012).
27. J. Miao, T. Ishikawa, I. K. Robinson, and M. M. Murnane, "Beyond crystallography: Diffractive imaging using coherent X-ray light sources," *Science* **348**(6234), 530–535 (2015).
28. J. Miao, P. Charalambous, J. Kirz, and D. Sayre, "Extending the methodology of X-ray crystallography to allow imaging of micrometre-sized non-crystalline specimens," *Nature* **400**(6742), 342–344 (1999).
29. J. N. Clark, X. Huang, R. Harder, and I. K. Robinson, "High-resolution three-dimensional partially coherent diffraction imaging," *Nat. Commun.* **3**(1), 993 (2012).
30. B. Whetten, "Supplemental information - computer code: Phasecorrection2dv9," figshare (2021), <https://doi.org/10.6084/m9.figshare.16881787>.
31. C. C. Chen, J. Miao, C. W. Wang, and T. K. Lee, "Application of optimization technique to noncrystalline x-ray diffraction microscopy: Guided hybrid input-output method," *Phys. Rev. B* **76**(6), 064113 (2007).